

# Efficient Three-Dimensional Imaging From a Small Cylindrical Aperture

Mark A. Haun, Douglas L. Jones, and William D. O'Brien, Jr.  
Department of Electrical and Computer Engineering  
University of Illinois at Urbana-Champaign

**Corresponding author:** Mark Haun (contact info below)

This work was supported by NIH grant CA79179.

Mark A. Haun  
111 Coord. Science Lab, MC-228  
1308 W. Main St.  
Urbana, IL 61801  
(217) 244-0575 (voice)  
(217) 244-1642 (fax)  
markhaun@uiuc.edu

Douglas L. Jones  
Coordinated Science Lab  
1308 W. Main St.  
Urbana, IL 61801  
(217) 244-6823 (voice)  
(217) 244-1642 (fax)  
dl-jones@uiuc.edu

William D. O'Brien, Jr.  
4255 Beckman Institute, MC-251  
405 N. Matthews  
Urbana, IL 61801  
(217) 333-2407  
(217) 244-0105  
wdo@uiuc.edu

## Abstract

Small-diameter cylindrical imaging platforms, like those being considered in the development of *in vivo* ultrasonic microprobes, pose unique image formation challenges. The curved apertures they provide are incompatible with many of the commonly used frequency-domain synthetic aperture imaging algorithms. At the same time, their frequently small diameters place limits on the available aperture and the angular resolution that may be achieved. We obtain a three-dimensional, frequency-domain imaging algorithm for this geometry by making suitable approximations to the point spread function for wave propagation in cylindrical coordinates and obtaining its Fourier transform by analogy with the equivalent problem in Cartesian coordinates. For the most effective use of aperture, we propose using a focused transducer to place a virtual source a short distance from the probe. The focus is treated as a diverging source by the imaging algorithm, which then forms images on deeper cylindrical shells. This approach retains the simplicity and potential angular resolution of a single element, yet permits full use of the available probe aperture and a higher energy output. Computer simulations and experimental results using wire targets show that this imaging technique attains the resolution limit dictated by the operating wavelength and the transducer characteristics.

# 1 Introduction

An ongoing research project is developing very small ultrasound transducers that can be fabricated on the side of a needle and operated *in vivo* at high frequencies. Such probes could eventually provide a minimally invasive alternative to biopsy and speed the diagnosis of tumors. Crucial to the success of this effort are imaging algorithms adapted to the geometry imposed by these ultrasonic microprobes [1].

This image formation problem is challenging due to the microprobes' shape. With one probe, only two transducer motions are possible: inward and outward travel, and rotation about the needle axis. The imaging aperture is therefore highly curved and its spatial extent is severely limited. Because the microprobe transducer will be surrounded by a scattering volume, good resolution in three dimensions is desirable so that quality 2-D image slices may be obtained. This can be accomplished using synthetic aperture techniques, but a significant 2-D aperture is required. It is imperative, then, that the available probe diameter be used efficiently.

Many of these constraints also apply to other imaging systems. Some intravascular ultrasound (IVUS) systems, for example, use a circular array of transducers on a catheter to image the interior of blood vessels [2]. As new ultrasound imaging modalities are developed, it is anticipated that cylindrical apertures will become more common and will benefit from ongoing work in this area.

## 2 Synthetic aperture imaging in a cylindrical geometry

Circular apertures have previously been used for intravascular ultrasound (IVUS) imaging systems, where synthetic aperture or array focusing has usually been carried out in the time domain [2, 3]. Frequency-domain algorithms, however, have a large speed advantage over

traditional beamforming methods due to the computational efficiency of the Fast Fourier Transform [4]. (The computational requirements of conventional beamforming and the proposed frequency-domain algorithm are compared at the end of this section.)

A frequency-domain imaging method was recently proposed for use with IVUS systems [5]. The authors start with a geometrically derived, two-dimensional point spread function (PSF) and obtain the Fourier transform of the imaging kernel for monostatic (co-located transmitter and receiver) and bistatic cases using the method of stationary phase.

In the following derivation, the PSF for three-dimensional, monostatic imaging from a cylindrical aperture is obtained using the Rayleigh-Sommerfeld formulation of scalar diffraction theory. This PSF is then compared with the PSF for wave propagation in Cartesian coordinates, which has a well-known Fourier transform. This approach makes clear the narrow-beamwidth approximation necessary to put the PSF for cylindrical coordinates into the same form and obtain its Fourier transform. Because of the monostatic imaging assumption, the resulting algorithm is best-suited to applications where it is only practical to have a single-element transducer.

We start with the Rayleigh-Sommerfeld formula [6],

$$U(P_0) = \int \int_{\Sigma} \frac{1}{j\lambda} U(P_1) \frac{e^{jkr_{01}}}{r_{01}} \cos(\vec{n}, \vec{r}_{01}) ds \quad (1)$$

which expresses the field at  $P_0$ , located on the imaging aperture, in terms of a source distribution on the surface  $\Sigma$  shown in Figure 1. Given monostatic data acquisition in a constant-velocity, weakly scattering medium, no generality is lost by considering the scatterers on  $\Sigma$  to be the original source of ultrasonic waves traveling at speed  $c/2$ ; this is the “exploding reflectors” model sometimes used in exploration seismology [7]. Rewriting (1) using cylindrical coordinates, we have

$$\begin{aligned}
U(R, \phi, z) &= \int_{-\infty}^{\infty} \int_{-\pi}^{\pi} \frac{1}{j\lambda} U(r_i, \phi_i, z_i) \\
&\cdot \frac{\exp(jk\sqrt{R^2 + r_i^2 - 2Rr_i \cos(\phi - \phi_i) + (z - z_i)^2})}{R^2 + r_i^2 - 2Rr_i \cos(\phi - \phi_i) + (z - z_i)^2} \\
&\cdot (r_i - R \cos(\phi - \phi_i)) r_i d\phi_i dz_i .
\end{aligned} \tag{2}$$

This is a convolution integral; the point spread function is

$$\begin{aligned}
h(\phi, z) &= \frac{1}{j\lambda} (r_i - R \cos \phi) r_i \\
&\cdot \frac{\exp(jk\sqrt{R^2 + r_i^2 - 2Rr_i \cos \phi + z^2})}{R^2 + r_i^2 - 2Rr_i \cos \phi + z^2} .
\end{aligned} \tag{3}$$

If the transducer beamwidth is not too wide, the cosine terms in the exponential and the denominator may be approximated to second order as  $1 - \phi^2/2$ . (For a justification and some analysis of this approximation, see Appendix A.) If the other cosine term in the numerator is approximated to first order, we have

$$\begin{aligned}
h(\phi, z) &\approx \frac{1}{j\lambda} (r_i - R) r_i \\
&\cdot \frac{\exp(jk\sqrt{(R - r_i)^2 + Rr_i\phi^2 + z^2})}{(R - r_i)^2 + Rr_i\phi^2 + z^2} .
\end{aligned} \tag{4}$$

Now compare (4) with the PSF obtained for a rectangular aperture in Cartesian coordinates:

$$h(x, y) = \frac{1}{j\lambda} \cdot \frac{d \exp(jk\sqrt{d^2 + x^2 + y^2})}{d^2 + x^2 + y^2} . \tag{5}$$

Clearly they have the same form, except that the angular variable is scaled by the geometric mean of the transducer and reflector radii. The Fourier transform of  $h(x, y)$  is well known [6], and the transform of  $h(\phi, z)$  follows easily using the scaling property:

$$H(f_\phi, f_z) \approx \sqrt{\frac{r_i}{R}} e^{j2\pi(r_i - R)\sqrt{\frac{1}{\lambda^2} - \frac{f_\phi^2}{Rr_i} - f_z^2}} \tag{6}$$

where the fact that  $\phi$  is an angular variable (and  $h(\phi, z)$  is thus periodic in  $\phi$ ) has been ignored, and  $\lambda = c/2f$  is in accordance with the exploding reflectors model.

In the spatial-frequency  $(f_\phi, f_z)$  domain, multiplication by  $H$  is equivalent to propagating the wave field from one concentric cylindrical surface to another. This is the principle behind what are known as *Fourier migration* algorithms in the seismic exploration community [8] and *wavenumber* or  $\omega - k$  algorithms in the radar community [9]. The most significant difference here is that now  $H$  is a function not only of the relative distance between the target and recording surfaces, but also of the absolute radii of those surfaces.

Following [10], a simple way to obtain a two-dimensional image at one desired depth is to first compute the 3-D FFT of the raw data, taking it into the  $(f_\phi, f_z, f)$  domain. Then, for each temporal frequency  $f$ , the  $(f_\phi, f_z)$  spatial frequency planes are multiplied by the appropriate  $H(f_\phi, f_z)$  for the target reconstruction depth. Finally, the resulting data cube is summed over temporal frequency  $f$ , and an inverse 2-D FFT yields the focused image. The required discretization of this process is straightforward, but the spatial sampling in  $\phi$  and  $z$  must be dense enough to prevent artifacts; an in-depth discussion of this issue may be found in [11].

In practice, if the full three-dimensional image is desired, the  $H$  operator will be applied repeatedly to back-propagate the wavefield in increments of the axial resolution. At each iteration, the data are summed over  $f$  and inverse transformed to yield the next cylindrical image slice. This is analogous to the seismic migration technique known as *phase-shift migration* [12].

To evaluate the computational efficiency of this approach, consider an experiment in which echoes are recorded at  $N_s \times N_s$  positions on a curved aperture. Let  $N_t$  time samples be recorded for each signal. The imaging algorithm will be tasked with computing  $N_s^2 N_t$  voxels in the target volume. Conventional beamforming is here viewed as a series of delay-and-sum operations on the raw  $(\phi, z, t)$  dataset. Operation counts for the frequency-domain algorithm follow directly from the steps described above. The results are listed in Table 1.

For the parameters used in the simulations and experiments of the following sections ( $N_s = 128$ ,

$N_t = 512$ ), conventional beamforming would require about  $1.4 \times 10^{11}$  real multiplies and adds. The proposed frequency-domain algorithm requires about  $1.8 \times 10^{10}$  multiplies and adds, a savings of 87%. While a host of implementation-dependent factors make it impossible to categorically declare one algorithm as “best,” the potential gains of working in the frequency domain are evident. Other factors which might favor a frequency-domain implementation are the ease of parallelizing the FFTs and the elimination of oversampling requirements.

### 3 Options for effective use of the available aperture

When a single-element, unfocused transducer is significantly larger than a wavelength and has an effective aperture  $D$ , the best lateral resolution available with synthetic aperture processing is approximately  $D/2$  [13]. For high-frequency ultrasound applications, this would seem to suggest using a transducer that is extremely small, on the order of one wavelength! Such a small transducer would place severe limits on the available pulse energy in an application where the low signal-to-noise ratio is already a major concern.

One possible solution is to use the full probe diameter for a focused transducer and treat the focus as a virtual source [14]. The virtual source traces out a cylindrical surface, as shown in Figure 2. The imaging algorithm proceeds as if there were an unfocused transducer located at the focus, treating that point as a source of diverging waves. It can then form images at depths past the real focus. A recent study exploring this technique found that the resolution achievable beyond the focus is comparable to the resolution at the focus, this fundamental limit being set by the focal ratio of the transducer [15].

Using a focused transducer to create a virtual source has the advantage that more transducer area, and hence more energy, is available for transmitting. It is important to realize, however, that we are not getting something for nothing: The usable aperture is still the same, even though

the virtual source may be traveling on a much larger surface. For a transducer of some constant diameter, as the focal length is increased, the width of the focal region increases and the beamwidth past the focus decreases. These factors conspire to limit the attainable resolution in the virtual source case.

## 4 Resolution

### 4.1 Axial Resolution

As in all pulse-echo imaging systems, the axial resolution is determined by the length of the pulse, although this may be shorter than the actual transmitted waveform if pulse compression is used. If the transmitted energy is uniform over a bandwidth  $W$ , the axial resolution (using the Rayleigh criterion) will be approximately

$$\delta_r = \frac{c}{2W} \quad (7)$$

corresponding to  $c/2$  times the interval from peak to first zero-crossing of the *sinc* function  $\sin(\pi Wt)/\pi t$ .

### 4.2 Lateral Resolution

The lateral resolution attainable in this imaging geometry is easiest to calculate when the transducer size is small compared to the wavelength. As the probe moves, the echoes from any given scattering point are phase modulated by the changing scatterer-transducer distance. The amount of phase modulation governs the extent of the data collected in the spatial frequency domain and hence the resolution. Larger transducers cause a smearing of the raw data that imposes a window on the data in the spatial frequency domain and degrades the resolution.

From Equation 2, the phase of the received signal at  $(R, \phi, z)$  due to a point reflector at  $(r_i, \phi_i, z_i)$

is, using the exact form of the distance function,

$$\psi(\phi, z) = 2\pi f \frac{2}{c} \sqrt{R^2 + r_i^2 - 2Rr_i \cos(\phi - \phi_i) + (z - z_i)^2}. \quad (8)$$

The spatial derivatives of this function yield the instantaneous spatial frequencies of the unprocessed data:

$$\begin{aligned} f_\phi &= \frac{1}{2\pi} \frac{d}{d\phi} \psi(\phi, z) \\ &= \frac{2f}{c} \cdot \frac{Rr_i \sin(\phi - \phi_i)}{\sqrt{R^2 + r_i^2 - 2Rr_i \cos(\phi - \phi_i) + (z - z_i)^2}} \\ |f_\phi|_{max} &= \frac{2R}{\lambda} \sin \frac{\gamma_{r\phi}}{2} \end{aligned} \quad (9)$$

where  $\gamma_{r\phi}/2$  is the half-beamwidth of the ultrasound transducer in the  $r\phi$  plane (see Figure 3).

We also have

$$\begin{aligned} f_z &= \frac{1}{2\pi} \frac{d}{dz} \psi(\phi, z) \\ &= \frac{2f}{c} \cdot \frac{z - z_i}{\sqrt{R^2 + r_i^2 - 2Rr_i \cos(\phi - \phi_i) + (z - z_i)^2}} \\ |f_z|_{max} &= \frac{2}{\lambda} \sin \frac{\gamma_{rz}}{2} \end{aligned} \quad (10)$$

where  $\gamma_{rz}/2$  is the half-beamwidth of the transducer in the  $rz$  plane.

We can now estimate the lateral resolution in the  $z$  and  $\phi$  directions for the case of a small transducer. The variation of  $f_z$  and  $f_\phi$  defines an approximate rectangle in the spatial frequency domain, symmetric about  $(f_\phi, f_z) = (0, 0)$ . Following [16], the resolution under the Rayleigh criterion is determined from the extent of the spatial frequency data as

$$\delta_\phi = \frac{\lambda}{4R \sin \frac{\gamma_{r\phi}}{2}} \text{ rad} = \frac{\lambda r_i}{4R \sin \frac{\gamma_{r\phi}}{2}} \text{ m at depth } r_i \quad (11)$$

$$\delta_z = \frac{\lambda}{4 \sin \frac{\gamma_{rz}}{2}} \text{ m} \quad (12)$$

What if the transducer is not small with respect to the wavelength? In this case, the aperture impulse response must be convolved with the transmitted pulse, which causes the spatial

frequency data to be windowed. See [13] for a detailed derivation of this effect. If the transducer has an effective aperture of  $D$ , then the lateral resolution will be approximately  $D/2$  (in the  $z$ -direction; the resolution in the  $\phi$ -direction is depth-dependent).

If the virtual source technique is used, calculation of the expected lateral resolution is more difficult because of the complex field pattern beyond the focus. The above formulas are not applicable, for they assume a relatively flat response within the transducer beamwidth and sharp cutoffs at angles of  $\pm\gamma_{r\phi}/2$  and  $\pm\gamma_{rz}/2$ , leading to a sinc-like response for point targets. For focused transducers, the natural apodization provided by the past-focus beam pattern will broaden the main lobe and reduce the sidelobes. Simulations and experiments have shown the achievable resolution to be about the same as the size of the focal region: approximately  $F\lambda$ , where  $F$  is the focused transducer’s focal ratio, or “f-number.”

## 5 Simulations

Two types of computer simulations were performed to verify the performance of this imaging method. In the first, an infinitesimally small, unfocused transducer was simulated to test the algorithm and its inherent approximations, independent of the virtual source technique. Five point reflectors in an “X” pattern at radius  $r_i = 15$  mm were imaged by a transducer at radius  $R = 8$  mm having a beamwidth of  $20^\circ$ . A Gaussian-weighted 5-MHz sinusoid with a 3-MHz bandwidth was used for the transmit pulse. Simulated echoes were collected on a 128x128 grid with  $\phi$  ranging from  $-55^\circ$  to  $+55^\circ$  and  $z$  ranging from  $-6.4$  to  $+6.4$  mm. These data were processed with the algorithm described in Section 2; Figure 4 shows the results. The lateral resolution is comparable to the values predicted by equations (11) and (12):  $3.1^\circ$  in  $\phi$  and 0.43 mm in  $z$ . Due to the lack of any apodization in the simulated beam pattern, high sidelobes are to be expected, and in fact the first sidelobes are only 22 dB down.

In the second type of simulation, the *Field II* program [17] was used to simulate a spherically focused transducer and thus validate the virtual source technique used in the experiments. Point reflectors at radius  $r_i = 57$  mm were imaged by an  $f/1.33$ , 19.1-mm diameter transducer at radius 22.3 mm, yielding a virtual source radius of  $R = 47.7$  mm. A Gaussian-weighted 2.25-MHz sinusoid with a half-power bandwidth of 1.1 MHz was used as the transmit pulse. Simulated echoes were collected on a 128x128 grid with a  $\phi$  step size of  $0.14^\circ$  and a  $z$  step size of  $120 \mu\text{m}$ . All of these parameters were selected to match as closely as possible the parameters of the first experiment described in the following section.

As can be seen in Figure 5, in this simulation the main lobe has broadened and the side lobes are lower, due to the tapering of the transducer beam pattern beyond the focus. The half-power resolution is about  $600 \mu\text{m}$ ; as expected, this is comparable to the width of the focal region.

## 6 Experimental results

A number of experiments were performed in a water tank with a precision positioning system and conventional focused ultrasound transducers in pulse-echo mode. In the first experiment, a 19.1-mm diameter, 2.25-MHz transducer with a measured focal length of 26.5 mm was mounted to a vertical support arm in the water tank and used to scan a target consisting of three  $100\text{-}\mu\text{m}$  wires crossing at the center of a plastic holder (Figure 6). The central part of the target was approximately 10 mm beyond the focus of the transducer. The transducer was scanned up and down and rotated about the axis of its support arm, covering an area of 15.4 mm by  $17.9^\circ$  in 128 by 128 steps.

After processing, “fly-through” movies were generated showing the imaged wires on a series of cylindrical shells. Reflections are present over a range of depths because the imaging cylinder cuts through the planar target at different places depending on the depth chosen for focusing. To

create the right-hand panel in Figure 7, these images were summed over depth, creating a 2-D projection with a complete view of the target. Compare the detail visible in this image with that in the left-hand panel, which was obtained from the raw echoes by an absolute summation of the received waveform at each scan location. Figure 8 plots the one-dimensional profiles across the in-focus wires at two different reconstruction depths. The measured half-power [synthesized] beamwidth at the target distance is about  $600 \mu\text{m}$  in either the  $z$  or  $\phi$  directions, due to the choice of step sizes and distance to the target. This compares favorably to the transducer's resolution at focus, and is in excellent agreement with the *Field II* simulation of Section 5.

In another experiment, a 15-MHz transducer having a 12.7-mm diameter, a 19.1-mm focal length, and a theoretical resolution at focus of  $\lambda D/f = 150 \mu\text{m}$  was used. The target was a piece of ordinary 1.6-mm aluminum screen held at constant radius from the transducer support arm and about 5 mm beyond the focus of the transducer (see Figure 9). The area scanned for this experiment was 6.4 mm by  $8.32^\circ$  in 128 by 128 steps.

Figure 10 shows two log-scaled images of the wire screen, at distances of 5.17 mm and 5.30 mm beyond the focus of the transducer. The mesh consists of vertical wires that are nearly straight, parallel, and normal to the view direction, and horizontal wires which weave through them. The upper image shows some of the vertical wires and also the over-crossings of the horizontal wires. In the lower image, the deeper focus reveals other vertical wires, indicating that the wire mesh was held at a not-quite-constant radius. Most of the wire over-crossings are still visible, but the rest of the horizontal wires remain invisible due to their angles with respect to the view direction (note that the wire diameter, at  $280 \mu\text{m}$ , is much larger than the acoustic wavelength).

## 7 Conclusions

An efficient and accurate three-dimensional image formation algorithm has been obtained directly through simple approximations to the point spread function for 3-D wave propagation in cylindrical coordinates. Computer simulations and experimental results verify its good performance. When combined with the virtual source technique, this algorithm should allow high quality, near-diffraction-limited imaging from small cylindrical platforms, whether they be needles, catheters, or others yet to be developed.

The authors thank Rita Miller and Bill Zierfuss of the Bioacoustics Research Laboratory for providing instruction and assistance in laboratory procedures. They also thank the reviewers for helping improve the quality of this paper.

## A Validity of the approximate distance function

The narrow-beamwidth approximation  $\cos \phi \approx 1 - \phi^2/2$  will now be examined in more detail. The square-root quantity being approximated in (2) is  $r_{01}$ , the distance from the transducer to a reflector in the scattering volume, expressed in cylindrical coordinates. Set  $z = z_i = 0$  and consider the angle range,  $\pm\phi$ , over which echoes may be collected from a point reflector at radius  $r_i$ . From Figure 3,  $\phi$  is related to the transducer beamwidth  $\gamma_{r\phi}$  by

$$\frac{r_i \sin \phi}{\sqrt{R^2 + r_i^2 - 2Rr_i \cos \phi}} = \sin \frac{\gamma_{r\phi}}{2} . \quad (13)$$

This is a quadratic equation in  $\cos \phi$ ; the solution (assuming all angles are in the first quadrant) is

$$\phi = \arccos \left( \frac{R \sin^2 \frac{\gamma_{r\phi}}{2} + \cos \frac{\gamma_{r\phi}}{2} \sqrt{r_i^2 - R^2 \sin^2 \frac{\gamma_{r\phi}}{2}}}{r_i} \right) . \quad (14)$$

A simple (though computationally demanding) reconstruction method from synthetic aperture data is to back-project the time series recorded at each transducer position, smearing the data

back onto the loci of constant travel time in the target space. Even though the imaging algorithm proposed here operates in the Fourier domain, simple back-projection is a useful concept for understanding the effects of the distance approximation (see Figure 11).

The validity of the narrow-beamwidth approximation may be tested for a given cylindrical imaging problem by imposing a limit on the distance error

$$\sqrt{(R - r_i)^2 + Rr_i\phi^2} - \sqrt{R^2 + r_i^2 - 2Rr_i \cos \phi} \leq K \quad (15)$$

with  $K = \lambda/2$ , for example. (For simplicity, it is assumed that  $z = z_i = 0$ .) Sample plots of the error (in wavelengths) versus the ratio  $r_i/R$  are given in Figure 12 for three different transducer beamwidths when  $R = 50\lambda$ , a typical value for the high-frequency ultrasonic microprobes being developed. Although the exact errors will be different for every cylindrical imaging scenario, the narrow-beamwidth approximation will usually break down only when the transducer beamwidth becomes extremely wide.

## References

- [1] M.A. Haun, D.L. Jones, and W.D. O'Brien, Jr., "Efficient three-dimensional imaging from a small cylindrical aperture," in *Proc. IEEE Ultrasonics Symposium*, San Juan, Puerto Rico, October 2000, pp. 1589–1592.
- [2] M. O'Donnell, M.J. Eberle, D.N. Stephens, J.L. Litzza, K. San Vicente, and B.M. Shapo, "Synthetic phased arrays for intraluminal imaging of coronary arteries," *IEEE Transactions on Ultrasonics, Ferroelectrics, and Frequency Control*, vol. 44, no. 3, pp. 714–721, May 1997.
- [3] M. O'Donnell, "Efficient synthetic aperture imaging from a circular aperture with possible application to catheter-based imaging," *IEEE Transactions on Ultrasonics, Ferroelectrics, and Frequency Control*, vol. 39, no. 3, pp. 366–380, May 1992.
- [4] M. Soumekh, *Synthetic Aperture Radar Signal Processing*, Wiley-Intersciences, New York, 1999.
- [5] D. Vray, C. Haas, T. Rastello, M. Krueger, E. Brusseau, K. Schroeder, G. Gimenez, and H. Ermert, "Synthetic aperture-based beam compression for intravascular ultrasound imaging," *IEEE Transactions on Ultrasonics, Ferroelectrics, and Frequency Control*, vol. 48, no. 1, pp. 189–201, January 2001.
- [6] J.W. Goodman, *Introduction to Fourier Optics*, McGraw-Hill, New York, second edition, 1996.
- [7] J.F. Claerbout, *Imaging the Earth's Interior*, Blackwell Scientific Publications, Palo Alto, 1985.
- [8] R.H. Stolt, "Migration by Fourier transform," *Geophysics*, vol. 43, pp. 23–48, 1978.

- [9] C. Cafforio, C. Prati, and E. Rocca, "SAR data focusing using seismic migration techniques," *IEEE Transactions on Aerospace and Electronic Systems*, vol. 27, no. 2, pp. 194–206, March 1991.
- [10] L.J. Busse, "Three-dimensional imaging using a frequency-domain synthetic aperture focusing technique," *IEEE Transactions on Ultrasonics, Ferroelectrics, and Frequency Control*, vol. 39, no. 2, pp. 174–179, March 1992.
- [11] P.T. Gough and D.W. Hawkins, "Imaging algorithms for a strip-map synthetic aperture sonar: Minimizing the effects of aperture errors and aperture undersampling," *IEEE Journal of Oceanic Engineering*, vol. 22, no. 1, pp. 27–39, January 1997.
- [12] J. Gazdag, "Wave equation migration with the phase-shift method," *Geophysics*, vol. 43, pp. 1342–1351, 1978.
- [13] P.T. Gough and D.W. Hawkins, "Unified framework for modern synthetic aperture imaging algorithms," *International Journal of Imaging Systems and Technology*, vol. 8, no. 4, pp. 343–358, 1997.
- [14] C. Passman and H. Ermert, "A 100-MHz ultrasound imaging system for dermatologic and ophthalmologic diagnostics," *IEEE Transactions on Ultrasonics, Ferroelectrics, and Frequency Control*, vol. 43, no. 4, pp. 545–552, July 1996.
- [15] C.H. Frazier and W.D. O'Brien, Jr., "Synthetic aperture techniques with a virtual source element," *IEEE Transactions on Ultrasonics, Ferroelectrics, and Frequency Control*, vol. 45, no. 1, pp. 196–207, January 1998.
- [16] D.C. Munson, Jr., J.D. O'Brien, and W.K. Jenkins, "A tomographic formulation of spotlight-mode synthetic aperture radar," *Proceedings of the IEEE*, vol. 71, no. 8, pp. 917–925, August 1983.

- [17] J.A. Jensen and N.B. Svendsen, “Calculation of pressure fields from arbitrarily shaped, apodized, and excited ultrasound transducers,” *IEEE Transactions on Ultrasonics, Ferroelectrics, and Frequency Control*, vol. 39, no. 2, pp. 262–267, March 1992.

## List of Tables

1	Computational cost of the proposed frequency-domain imaging algorithm compared to conventional focusing. . . . .	19
---	--	----

Table 1: Computational cost of the proposed frequency-domain imaging algorithm compared to conventional focusing.

Operation	Real multiplications	Real additions
(Conventional beamforming)		
Delay and sum $N_s^2$ elements, $N_s^2 N_t$ times	$N_s^4 N_t$	$N_s^4 N_t$
(Proposed algorithm)		
3-D FFT	$2N_s^2 N_t(2 \log_2 N_s + \log_2 N_t)$	$3N_s^2 N_t(2 \log_2 N_s + \log_2 N_t)$
Mult. by $H$ , $N_t$ times	$4N_s^2 N_t^2$	$2N_s^2 N_t^2$
Sum over $f$ , $N_t$ times	0	$2N_s^2 N_t^2$
2-D FFT, $N_t$ times	$4N_s^2 N_t \log_2 N_s$	$6N_s^2 N_t \log_2 N_s$
<b>Total</b>	$2N_s^2 N_t(2N_t + 4 \log_2 N_s + \log_2 N_t)$	$3N_s^2 N_t(\frac{4}{3}N_t + 4 \log_2 N_s + \log_2 N_t)$

## List of Figures

1	Cylindrical geometry for derivation of the point-spread function (PSF). . . . .	22
2	Using a focused transducer to create a virtual source element. . . . .	23
3	Transducer beamwidth in relation to the positions of the transducer and target in cylindrical coordinates . . . . .	24
4	Five point-reflectors at $r_i = 15$ mm imaged with an infinitesimally small transducer at $R = 8$ mm: Focused image (left) and slice at constant $\phi$ (right). . . . .	25
5	Five point-reflectors at $r_i = 57$ mm imaged using the virtual source technique with a [simulated] spherically focused transducer at $R = 22.3$ mm: Focused image (left) and slice at constant $\phi$ (right). . . . .	26
6	100- $\mu$ m wire target (left) and close-up (right). . . . .	27
7	Results of imaging a 100- $\mu$ m wire target located beyond the transducer focus: Raw echoes summed absolutely over time (left); stack of focused images summed absolutely over depth (right). . . . .	28
8	One-dimensional profiles of cuts across the in-focus wires taken at different reconstruction depths and wire orientations. At the depths being considered, the linear distance scale is approximately the same on both the $z$ and $\phi$ axes. . . . .	29
9	Experimental set-up showing transducer and wire mesh phantom. . . . .	30
10	Reconstructed images of wire mesh at 5.17 mm (top) and 5.30 mm (bottom) beyond the transducer's focus. . . . .	31
11	The effects of the second-order cosine approximation may be visualized by considering circles of constant travel time. Here, a circular wavefront departing $R = 2$ , $\phi = 0$ at $t = 0$ is shown at $ct = 1.5$ using the exact (dashed line) and approximate (solid line) forms of the distance function. The close match at small angles is evident. . . .	32

12 Error analysis for the second-order cosine approximation. These curves are plotted  
for transducer beamwidths of  $30^\circ$ ,  $60^\circ$ , and  $90^\circ$  when  $R = 50\lambda$ . . . . . 33

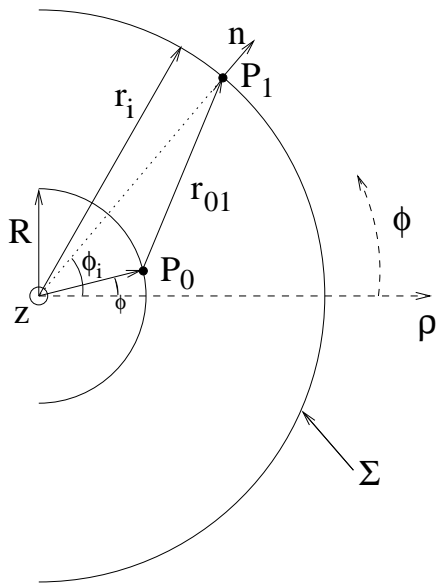


Figure 1: Cylindrical geometry for derivation of the point-spread function (PSF).

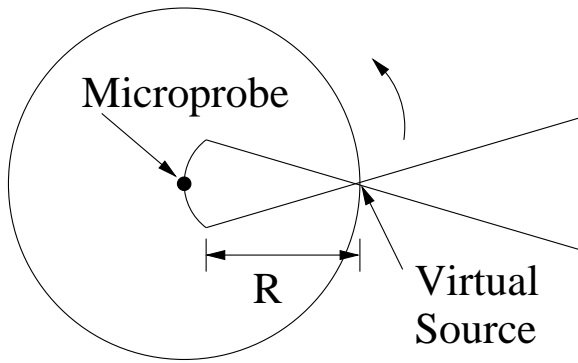


Figure 2: Using a focused transducer to create a virtual source element.

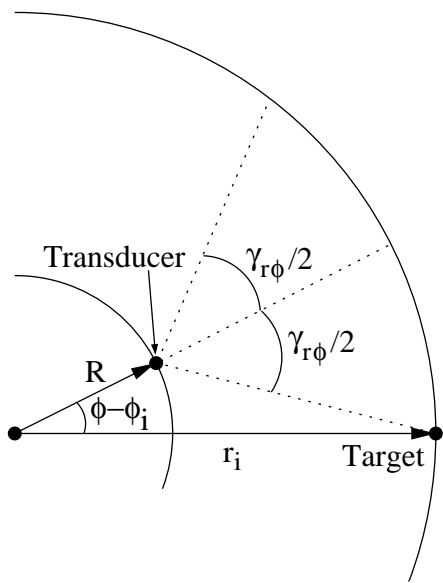


Figure 3: Transducer beamwidth in relation to the positions of the transducer and target in cylindrical coordinates

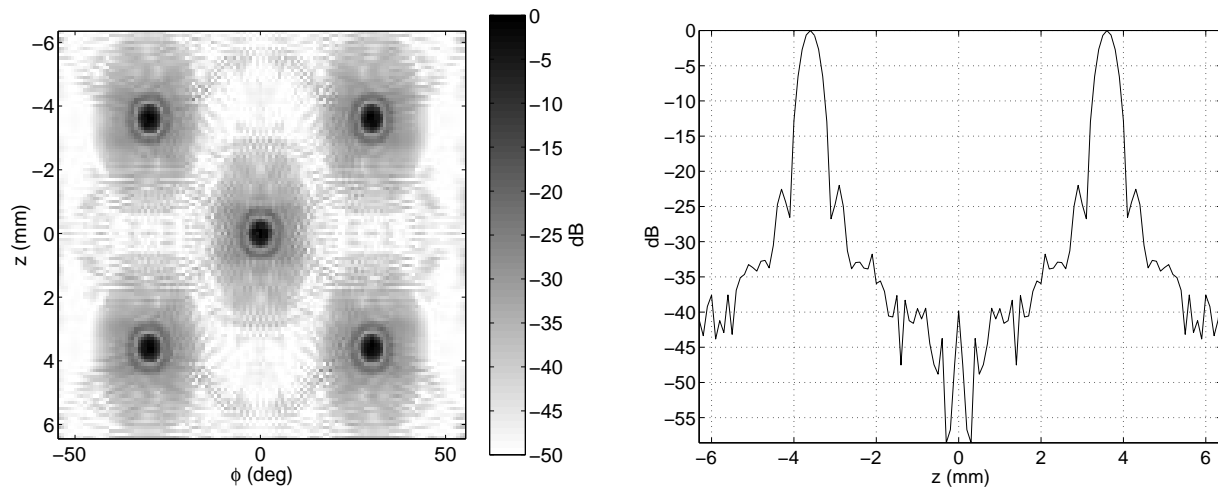


Figure 4: Five point-reflectors at  $r_i = 15$  mm imaged with an infinitesimally small transducer at  $R = 8$  mm: Focused image (left) and slice at constant  $\phi$  (right).

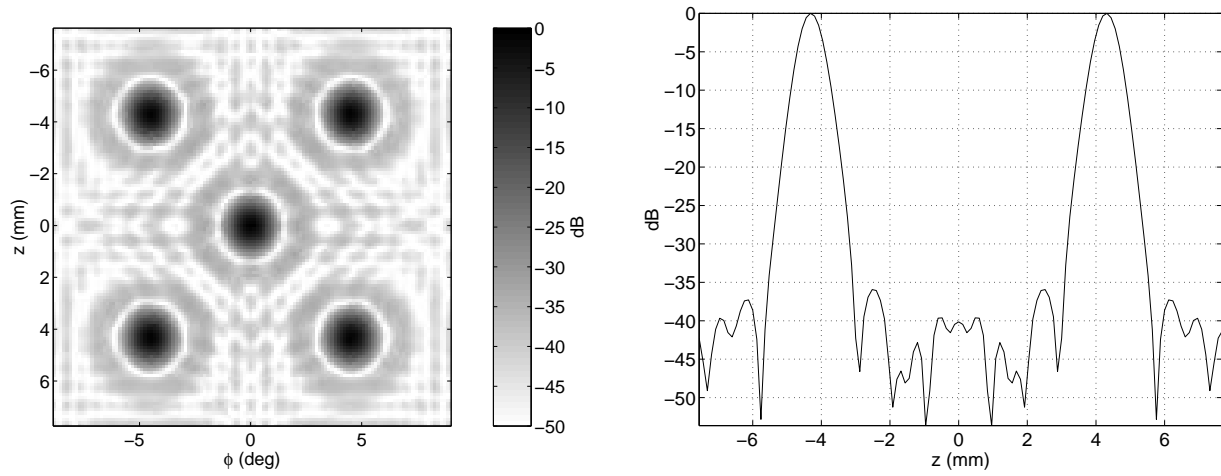


Figure 5: Five point-reflectors at  $r_i = 57$  mm imaged using the virtual source technique with a [simulated] spherically focused transducer at  $R = 22.3$  mm: Focused image (left) and slice at constant  $\phi$  (right).

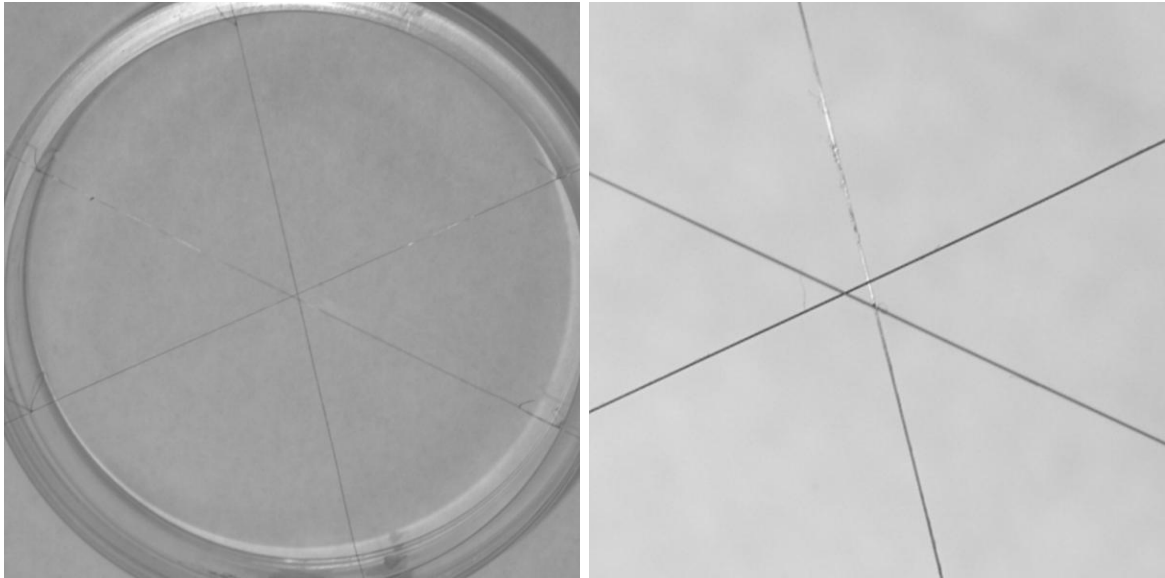


Figure 6: 100- $\mu\text{m}$  wire target (left) and close-up (right).

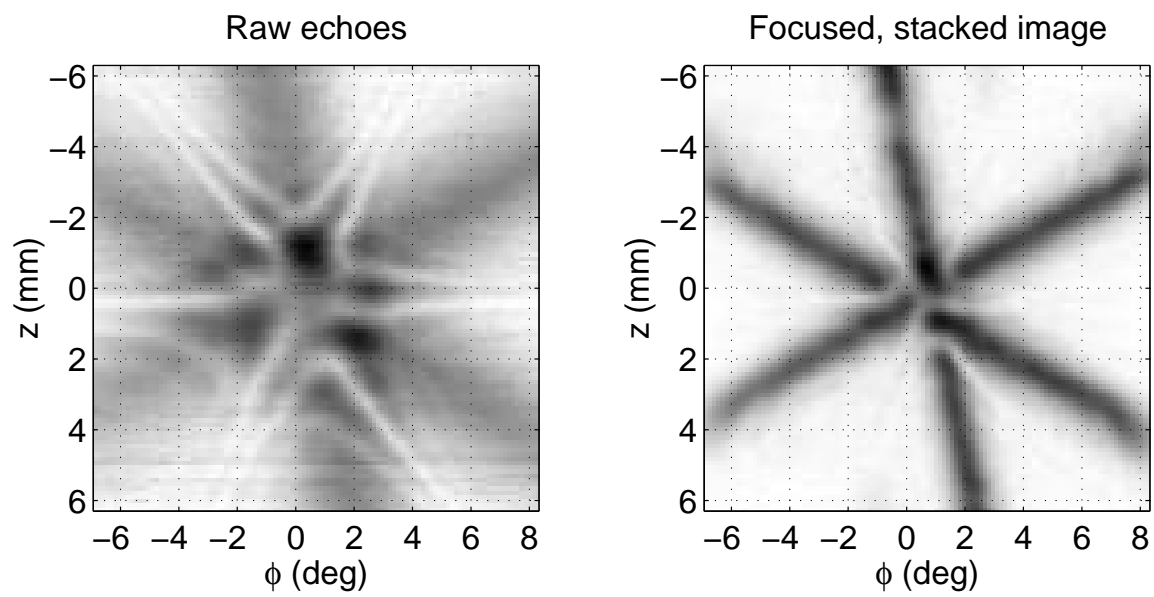


Figure 7: Results of imaging a 100- $\mu\text{m}$  wire target located beyond the transducer focus: Raw echoes summed absolutely over time (left); stack of focused images summed absolutely over depth (right).

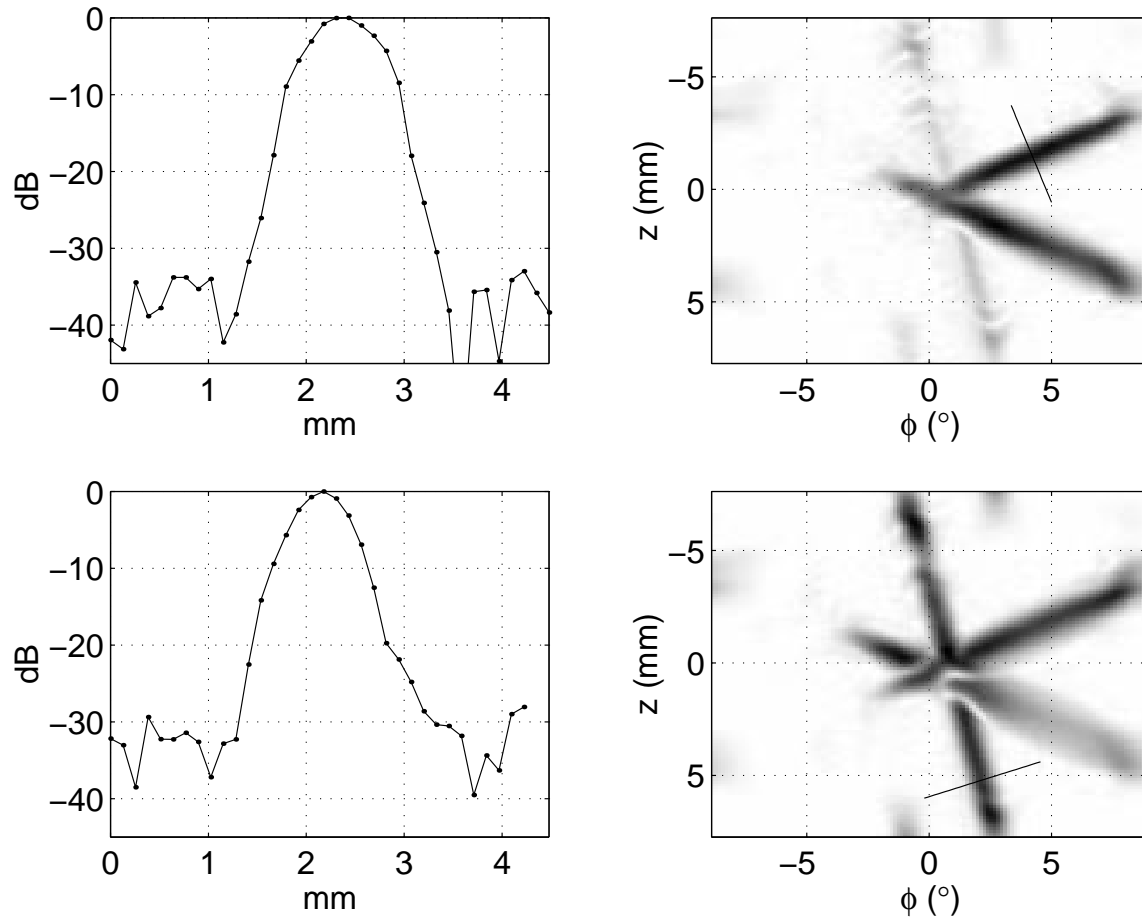


Figure 8: One-dimensional profiles of cuts across the in-focus wires taken at different reconstruction depths and wire orientations. At the depths being considered, the linear distance scale is approximately the same on both the  $z$  and  $\phi$  axes.

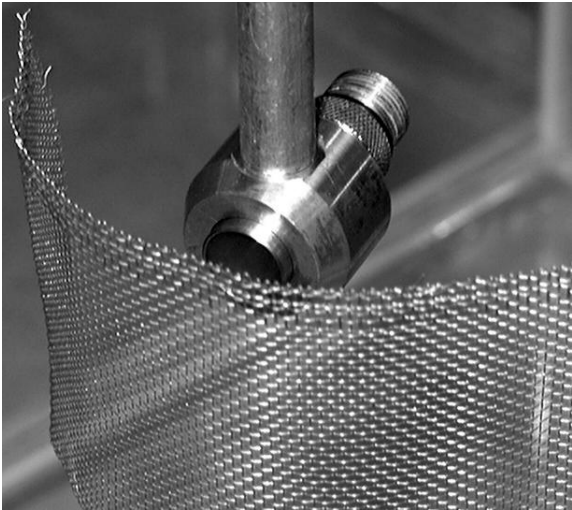


Figure 9: Experimental set-up showing transducer and wire mesh phantom.

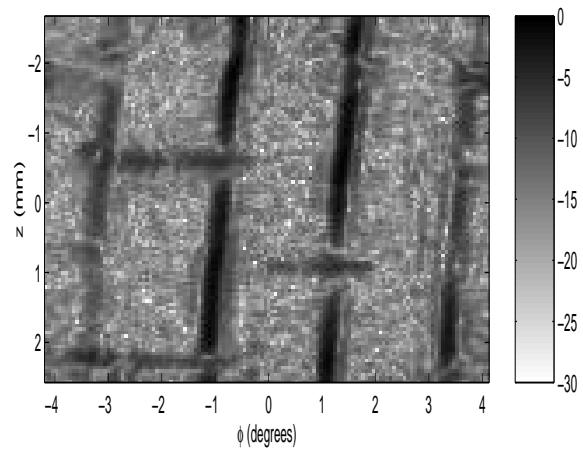
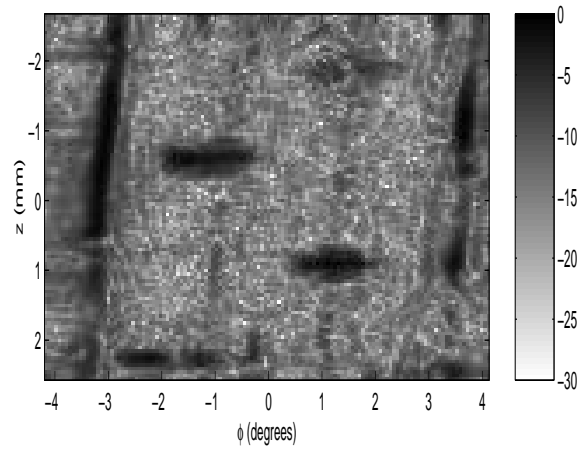


Figure 10: Reconstructed images of wire mesh at 5.17 mm (top) and 5.30 mm (bottom) beyond the transducer's focus.

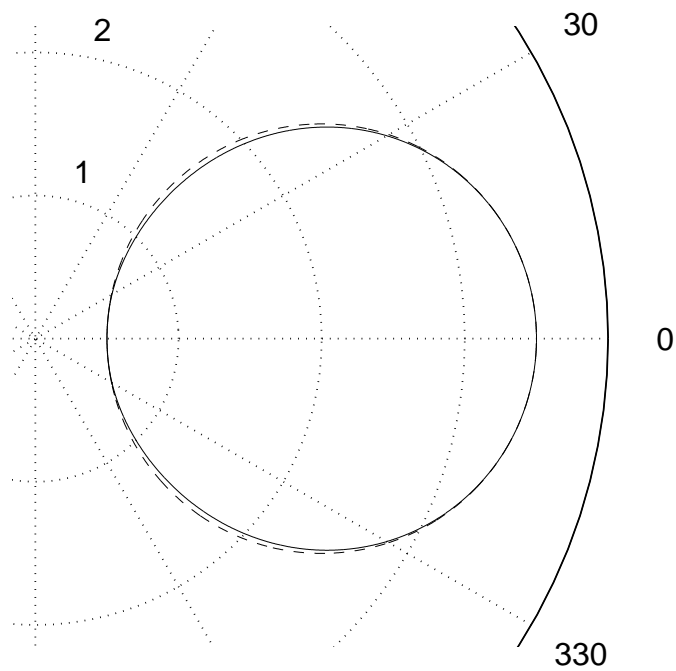


Figure 11: The effects of the second-order cosine approximation may be visualized by considering circles of constant travel time. Here, a circular wavefront departing  $R = 2$ ,  $\phi = 0$  at  $t = 0$  is shown at  $ct = 1.5$  using the exact (dashed line) and approximate (solid line) forms of the distance function. The close match at small angles is evident.

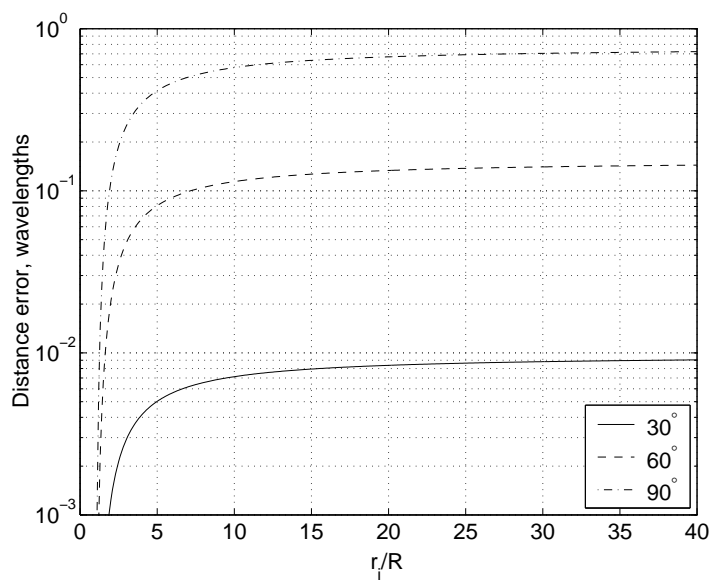


Figure 12: Error analysis for the second-order cosine approximation. These curves are plotted for transducer beamwidths of  $30^\circ$ ,  $60^\circ$ , and  $90^\circ$  when  $R = 50\lambda$ .